Journal of Materials Research and Technology 41 (2026) 1716–1726

Contents lists available at ScienceDirect

Journal of Materials Research and Technology

journal homepage: www.elsevier.com/locate/jmrt

Processing–microstructure–transport correlations in Y-358 ceramics: Effects of low-level Co substitution under optimized thermal conditions

Ryad Alhadei Mohamed Arebat [a,b,*], Mohd Mustafa Awang Kechik [a,**], Yap Siew Hong [a], Mustafa Mousa Dihom [c], Moftah Ben Yazid [c], Chen Soo Kien [a], Lim Kean Pah [a], Mohd Khalis Abdul Karim [a], Mohd Hafiz Mohd Zaid [a], Özgür Öztürk [d]

[a] Superconductor & Thin Films Laboratory, Department of Physics, Faculty of Science, Universiti Putra Malaysia, UPM, Serdang, Selangor, 43400, Malaysia
[b] Department of Physics, Faculty of Science, El-Mergib University, Al Khums, City, Libya
[c] Department of Physics, Faculty of Sciences, Alasmarya Islamic University, Zliten City, Libya
[d] Department of Electrical and Electronics Engineering, Kastamonu University, 37150, Kastamonu, Turkey

ARTICLE INFO

Handling Editor: SN Monteiro

Keywords:
Y-358 ceramic
Co-substitution
Microstructure evolution
Superconducting transport
Critical current density

ABSTRACT

This study examines the processing–microstructure–transport relationships in $Y_3Ba_5Cu_{8-x}Co_xO_{18-\delta}$ (Y-358) bulk ceramics synthesized via the solid-state reaction method, with emphasis on the influence of low-level cobalt substitution (x = 0.00–0.05). X-ray diffraction confirmed the orthorhombic Y-358 phase for all compositions. Microstructural analysis showed that light Co substitution (x = 0.01–0.03) improved grain alignment and densification, promoting stronger intergranular contact, whereas excessive substitution (x = 0.05) introduced porosity, microcracks, and disrupted grain connectivity. Electrical resistivity measurements revealed superconducting transitions across all samples, with the undoped composition exhibiting $T_{c\text{-onset}}$ ~93 K and $T_{c\text{-zero}}$ ~86 K. The optimally substituted sample (x = 0.03) demonstrated enhanced grain connectivity and a sharp single-step transition, indicating well-established intergranular coupling. Magnetic hysteresis measurements at 20 K further verified enhanced flux pinning for this composition, yielding a critical current density of 28.25 kA/cm^2 compared with 21.20 kA/cm^2 for the undoped sample (~33 % improvement). These findings demonstrate that controlled low-level Co substitution, combined with optimized thermal processing, provides an effective route to improve phase stability, microstructural refinement, flux pinning, and current-carrying capability in Y-358 ceramics, offering a practical pathway for advancing cuprate superconductor performance.

1. Introduction

High-temperature cuprate superconductors derive their performance from the delicate interplay between lattice structure, oxygen stoichiometry, and microstructural coherence, all of which regulate charge-carrier density, grain-boundary transport, and vortex dynamics [1–5]. For bulk ceramics, achieving high T_c and strong current-carrying capability requires precise control over thermal processing and dopant incorporation, as even subtle perturbations in the CuO_2 planes or Cu–O chain ordering can substantially alter the electronic landscape [6–8]. Among these systems, the higher-order $Y_3Ba_5Cu_8O_{18}$ (Y-358) phase, characterized by its extended *c*-axis and multiple CuO_2 layers, offers promising intrinsic properties but remains highly sensitive to processing conditions and chemical modification [9–11]. Despite this potential, the structure-property relationships governing doped Y-358 ceramics are still insufficiently understood. This study addresses this gap by examining how controlled Co substitution, combined with optimized calcination, sintering, and oxygenation, governs structural evolution, microstructural refinement, and superconducting transport in Y-358.

Within the broader Y–Ba–Cu–O (YBCO) family, interest has expanded beyond the widely studied $YBa_2Cu_3O_{7-\delta}$ (Y-123) phase to more complex homologues such as $YBa_2Cu_4O_8$ (Y-124), $Y_2Ba_4Cu_7O_{15}$ (Y-247), and notably, Y-358 [12–15]. The Y-358 structure contains five CuO_2 planes and three CuO chains per unit cell, resulting in a *c*-axis nearly three times longer than that of Y-123. Theoretical studies predict a T_c near 92 K for this phase; however, its superconducting response

* Corresponding author. Superconductor & Thin Films Laboratory, Department of Physics, Faculty of Science, Universiti Putra Malaysia, UPM, Serdang, Selangor, 43400, Malaysia.
** Corresponding author.
E-mail addresses: riadalhadearebat@gmail.com (R.A. Mohamed Arebat), mmak@upm.edu.my (M.M. Awang Kechik).

https://doi.org/10.1016/j.jmrt.2025.12.212
Received 5 November 2025; Received in revised form 15 December 2025; Accepted 20 December 2025
Available online 24 December 2025

remains highly sensitive to synthesis conditions, oxygen ordering, and dopant chemistry [7,16–19]. These characteristics make Y-358 a compelling but challenging system in which to tune superconductivity through deliberate compositional and microstructural engineering.

Cation substitution at the Cu site is a well-established approach for tuning hole concentration, lattice stability, and grain-boundary behavior in cuprate superconductors. Among available dopants, cobalt (Co) is particularly advantageous due to its multivalent states (Co^{2+}/Co^{3+}), slightly smaller ionic radius (0.69 Å vs. 0.73 Å for Cu^{2+}), and its active involvement in the electronic ^{structure} of the CuO_2 planes [20–23]. Unlike non-magnetic ions such as Zn^{2+} or Mg^{2+}, which primarily act as strong scattering centers that destabilize CuO_2 bonding, collapse anti-bonding states, and induce highly non-uniform hole distributions that rapidly suppress superconductivity [24], Co enables controlled modification of carrier density. Its partially filled 3d configuration introduces localized magnetic interactions that can reinforce flux pinning and stabilize grain-boundary coupling [25–27]. These combined electronic and structural attributes make Co a strategically effective dopant for probing and enhancing superconducting behavior in complex cuprate phases such as Y-358, where the balance among lattice strain, carrier density, and intergranular coherence is especially critical.

Earlier studies have reported that low Co substitution can refine grain morphology and induce mild lattice modifications, whereas excessive substitution tends to increase carrier scattering, generate microstrain, and suppress superconductivity. In Y-358, Co incorporation has been associated with changes in lattice dimensions and microstructure and with a reduction in Tc at higher doping levels [20,21,24]. In Y-358, Co incorporation has been associated with changes in lattice dimensions and microstructure and with a reduction in T_c at higher doping levels [22]. However, most available reports rely on non-optimized thermal processing routes and do not provide a unified interpretation linking dopant chemistry, lattice distortion, microstructure, and superconducting performance. Consequently, the combined influence of precise Co substitution and optimized synthesis conditions on the structural, transport, and magnetic properties of Y-358 remains largely unexplored.

Motivated by these gaps, the present work systematically investigates the effects of Co substitution (x = 0.00, 0.01, 0.03, 0.05) under optimized calcination, sintering, and oxygenation conditions on the phase formation, microstructure, electrical transport, and magnetic behavior of $Y_3Ba_5Cu_{8-x}Co_xO_{18-\delta}$ ceramics synthesized via the solid-state reaction method. Phase evolution is examined using X-ray diffraction (XRD), microstructural and compositional characteristics are evaluated through FESEM/EDX, superconducting transitions are assessed via four-point probe (4 PP) measurements, and flux-pinning behavior is quantified using vibrating-sample magnetometry (VSM) and the Bean model. To the best of our knowledge, this study provides the first comprehensive correlation between controlled Co doping, optimized thermal processing, and the resulting improvements in microstructural refinement, flux-pinning capability, and both resistive and magnetic superconducting performance in the Y-358 phase.

2. Experimental process

2.1. Sample preparation

Bulk ceramic samples of $Y_3Ba_5Cu_{8-x}Co_xO_{18-\delta}$ (x = 0.00, 0.01, 0.03, and 0.05) were synthesized using the conventional solid-state reaction method, a widely adopted route for oxide-based superconductors due to its simplicity, reproducibility, and scalability [28–30]. High-purity precursor powders, including Y_2O_3 (99.99 %, Alfa Aesar), $BaCO_3$ (99.95 %, Alfa Aesar), CuO (99.99 %, Alfa Aesar), and cobalt nanopowder (325 mesh, 99.5 %, Alfa Aesar), were weighed according to the stoichiometric ratios required for the Y-358 phase. As illustrated in Fig. 1, the powders were manually ground in an agate mortar for ~90 min to ensure uniform mixing. The homogenized mixture was placed in

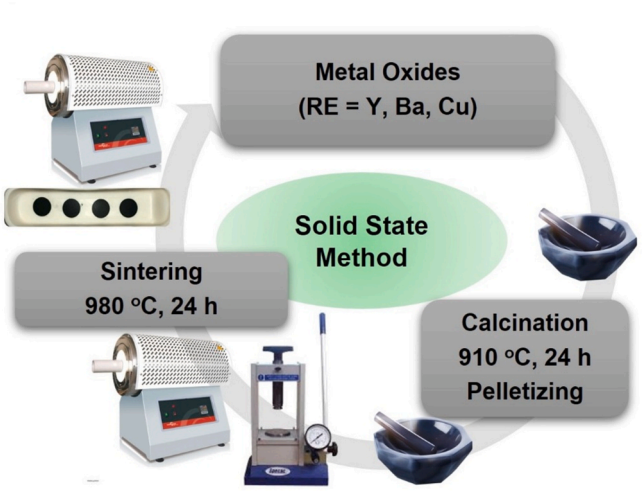

Fig. 1. The diagram depicts the procedure for preparing Y-358 bulk ceramics through the solid-state reaction (SSR) technique.

alumina crucibles and calcined at 910 °C for 24 h. To enhance phase homogeneity, the calcination step was repeated twice; after each cycle, the powders were reground for an additional 30 min. The resulting powders were uniaxially pressed into pellets (~11.5 mm diameter, ~1.5 mm thickness) under a pressure of 5 tons cm^{-2}. Sintering was conducted at 980 °C for 24 h in air near the onset of partial melting, consistent with reports indicating complete formation of the YBCO-related phase under these conditions [7,8]. During cooling, the samples were isothermally annealed at 600 °C for 12 h under flowing oxygen to promote oxygen diffusion and stabilize the orthorhombic structure [1,31]. This step was essential for achieving the required oxygen stoichiometry in Y-358. The final samples were designated Co-0.00, Co-0.01, Co-0.03, and Co-0.05 according to their respective Co substitution levels. This processing protocol was designed to optimize phase purity, densification, and microstructural integrity, ensuring reliable performance in subsequent structural and superconducting measurements.

A comparative summary of the thermal treatment parameters employed in this study versus those reported by Öztürk et al. (2019) is provided in Table 1, highlighting the optimization of calcination and sintering temperatures, as well as the extended annealing time under an oxygen-rich atmosphere.

2.2. Samples characterization

Phase identification and structural analysis were performed using X-ray diffraction (XRD) with a PW 3040/60 MPD X'Pert Pro Panalytical diffractometer (Cu–Kα radiation, λ = 1.5406 Å). Diffraction patterns were recorded over a 2θ range of 20°–80° to determine crystalline phases and evaluate lattice parameter variations resulting from Co

Table 1
Comparison of thermal processing conditions in this work and Öztürk et al. (2019), highlighting differences in temperature and oxygen annealing.

Processing Step	Temperature (°C)	Time (h)	Atmosphere	Repetitions	Ref.
Calcination	910	24	in air	one	This work
Sintering	980	24	in air	one	
Annealing	600	12	Oxygen flow	one	
Calcination	850	24	in air	Three	Ozturk et al. (2019)
Sintering	930	24	in air	one	
Annealing	500	5	Oxygen flow	one	

substitution. Surface morphology and elemental composition were examined using field-emission scanning electron microscopy (FESEM) equipped with an energy-dispersive X-ray spectrometer (EDX). These measurements provided information on grain structure, porosity, and the distribution of constituent elements. Superconducting transport properties were evaluated using the standard four-point probe (4 PP) technique, employing a Keithley 6221 DC current source and a Keithley 2182A nanovoltmeter. Measurements were conducted in a closed-cycle helium cryostat over a temperature range of 30–300 K. Magnetic measurements were carried out using a Lakeshore 7400-S vibrating sample magnetometer (VSM) at 20 K under an applied magnetic field of ±2 T. The resulting M − H hysteresis loops were used to assess diamagnetic response, flux-pinning behavior, and intergranular coupling. The width of the hysteresis loop (ΔM) provided insight into vortex dynamics and microstructural quality. The intragranular critical current density (J_c) was calculated from the magnetic hysteresis curves using the Bean critical-state model [32]:

$$J_c = \frac{20\Delta m}{a^2 d\left(b - \frac{a}{3}\right)} \quad (1)$$

where $\Delta M = M^+ - M^-$ is the separation between the upper and lower branches of the hysteresis loop, and a and b (a < b) are the in-plane dimensions of the sample, with thickness d included in the normalization factor.

3. Results and discussion

3.1. Crystal structure and phase formation analysis

Fig. 2(a) shows the X-ray diffraction (XRD) patterns of $Y_3Ba_5Cu_{8-x}Co_xO_{18-\delta}$ (x = 0.00, 0.01, 0.03, and 0.05) ceramics synthesized by solid-state reaction and annealed in flowing oxygen. All samples crystallize in the orthorhombic Y-358 phase with no detectable Co-rich impurities, confirming successful Co incorporation into the lattice [33,34]. Minor secondary peaks appear only in the undoped sample; however, their low intensity and non-superconducting nature indicate negligible influence on the observed superconducting transition [10,11,35]. The diffraction profiles in Fig. 2(b) reveal a systematic shift of reflections such as (108) and (018) toward lower 2θ angles with increasing Co content, indicating a slight lattice expansion.

Although Co^{3+} has a smaller ionic radius than Cu^{2+} (0.69 Å vs. 0.73 Å), its substitution introduces local structural distortion and promotes oxygen uptake to maintain charge neutrality, particularly in the CuO-chain regions [20,36–38]. Additional oxygen may occupy interstitial sites or modify bonding configurations, leading to elongation of the *c*-axis and increased microstrain, consistent with the observed peak shifts and broadening [1,39]. These structural trends were validated through Rietveld refinement using ICSD reference patterns and X'Pert HighScore Plus software [40,41], as listed in Table 2.

While the oxygen content (δ) was not directly measured in this study, indicators-*c*-axis expansion, orthorhombicity reduction, and increased peak broadening-are consistent with oxygen-incorporation effects often reported for YBCO systems [11]. It is also noteworthy that excessive oxygen flow during annealing can induce surface irregularities, abnormal grain coarsening, and oxygen-vacancy clustering, ultimately disrupting current pathways despite minimal changes in the XRD pattern [1]. Thus, precise control of oxygenation remains essential for optimizing Y-358's superconducting performance.

The lattice parameters *a* and *b* remain nearly unchanged across the series, whereas a modest and systematic increase in the *c*-axis is observed with higher Co content. This anisotropic expansion reflects the layered structure of Y-358, which comprises five CuO_2 planes and three CuO chains per unit cell [16,17,42]. Structural distortion was quantified using the orthorhombicity parameter [7,30]:

$$OT = (b - a)\backslash(b + a) \quad (2)$$

The low substitution level of x = 0.03 achieved precise structural modification, resulting in a controlled decrease in the orthorhombicity (from 0.0065 at x = 0.00 to 0.0053). This controlled shift subtly influences carrier scattering mechanisms and enhances phase stability, successfully optimizing the lattice environment for superconductivity [21,43]. Crucially, the Co-0.03 sample maintains high crystallinity and limits detrimental microstrain, unlike the high disorder observed at x = 0.05. This sustained high structural quality is vital for ensuring strong intergranular coupling and current path connectivity [11,17,42], with

Table 2
Presents the investigated samples' lattice parameters, orthorhombicity, and crystallite size.

Samples	*a*(Å)	*b*(Å)	*c*(Å)	(*c*/*a*) %	OT	Crystallite Size (Å)
Co-0.00	3.83	3.88	30.93	8.075	0.0065	224.6
Co-0.01	3.84	3.88	30.88	8.041	0.0052	233.7
Co-0.03	3.85	3.89	31.10	8.080	0.0053	240.2
Co-0.05	3.84	3.89	30.96	8.065	0.0065	304.1

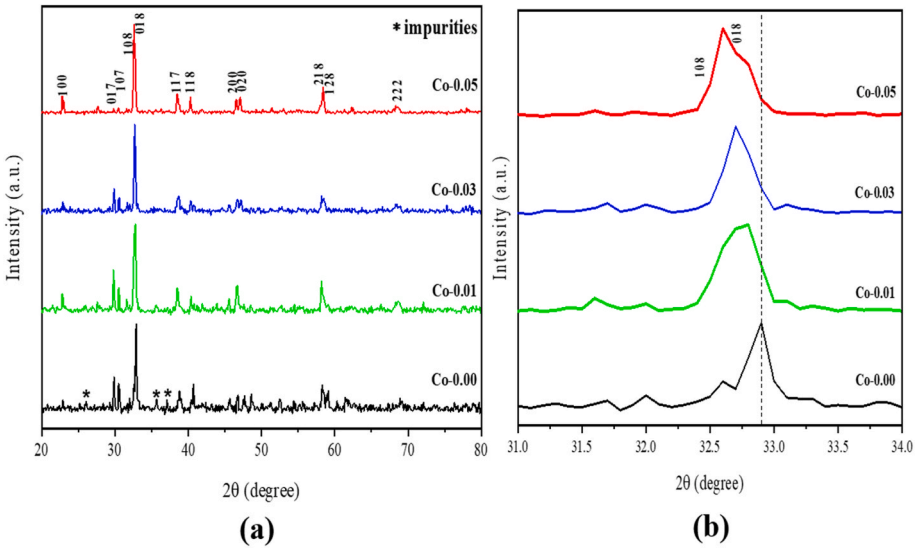

Fig. 2. (a) X-ray diffraction patterns with miller indices of Co-doped Y-358 bulk ceramics; (b) Characteristic (108) and (018) peaks of the Y-358 phase.

the resulting crystallite size being accurately quantified using the Scherrer equation:

$$L = k\lambda \backslash \beta \cos\theta \quad (3)$$

where $K = 0.9$, $\lambda = 0.154$ Å, β is the FWHM in radians, and θ is the Bragg angle. A modest increase in crystallite size is observed with low Co substitution (Table 2), suggesting improved localized alignment and particle coarsening, beneficial to current transport as long as excessive

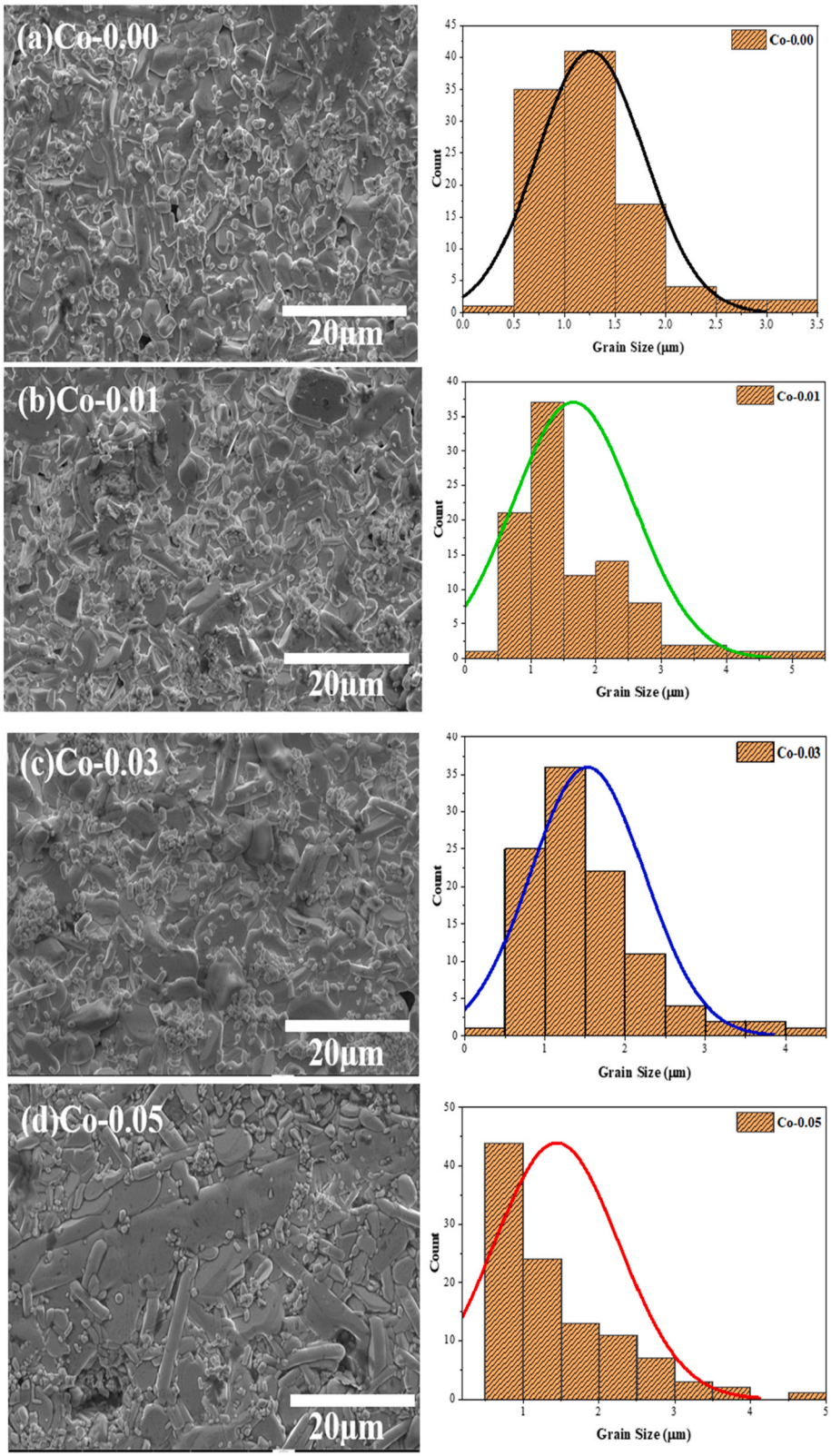

Fig. 3. (SEM) surface micrographs (a–d) illustrating the morphology of the synthesized Co-doped Y-358 bulk ceramic samples, accompanied by their respective grain size distribution histograms.

disorder is avoided [33,36].

In summary, the XRD analysis confirms that moderate Co substitution preserves the orthorhombic Y-358 structure while introducing controlled lattice distortion, particularly along the *c*-axis. These structural adjustments correlate well with the enhanced superconducting behavior observed in the optimally substituted samples, including the improved $T_{c\text{-onset}}$ (compared to Ozturk et al. (2019)) and the higher J_c demonstrated in later sections. In contrast, the x = 0.05 composition exhibits pronounced peak broadening, reduced orthorhombicity, and microstrain accumulation, indicating structural degradation that is fully consistent with its weakened superconducting response.

3.2. Microstructural analysis

Fig. 3(a–d) presents the SEM micrographs of $Y_3Ba_5Cu_{8-x}Co_xO_{18-\delta}$ (x = 0.00, 0.01, 0.03, and 0.05) ceramics, while the corresponding grain-size distributions are shown in Fig. 4(a). Grain size was evaluated by measuring approximately 100 grains per sample using ImageJ, and the results are summarized in Table 3 [44,45]. The undoped composition (x = 0.00) exhibited plate-like morphology with relatively uniform grains (~1.26 μm) and low porosity, consistent with the layered nature of REBCO systems [46]. Introducing a small amount of Co (x = 0.01) leads to noticeable grain coarsening (~1.65 μm), likely driven by enhanced diffusion kinetics and modified bonding environments introduced by Co–O interactions during sintering.

At x = 0.03, the microstructure becomes more refined and densely packed, displaying rectangular grains with improved intergranular contact and uniformly distributed nano-scale surface entities (Fig. 4(b)). Such features are frequently associated with enhanced connectivity pathways and reduced weak-link behavior in polycrystalline superconductors [31,47,48]. This morphology is consistent with the sharper superconducting transition and improved transport behavior observed for this composition.

Table 3
Average grain sizes for the produced samples of Co-doped Y-358 bulk ceramics.

Samples	Co-0.00	Co-0.01	Co-0.03	Co-0.05
Average Grain Sizes (μm)	~1.26	~1.65	~1.53	~1.54

In contrast, the x = 0.05 sample exhibited disordered grains with clustered nano-entities and spiral-like features, which can act as weak links and disrupt superconducting current pathways. Pronounced intergranular cracks indicated thermal stress and non-uniform oxygenation during post-annealing, both widely recognized as detrimental to current-carrying capacity in polycrystalline cuprates [2,21]. The abnormal grain growth, elevated porosity, and microcracks observed in Fig. 4(d) substantially increase grain-boundary energy and hinder the formation of continuous percolative paths. These microstructural defects directly explain the broadened superconducting transition and reduced T_c obtained for this composition [10,20]. Overall, the SEM analysis confirms that low-to-moderate Co substitution enhances grain packing and intergranular connectivity, whereas excessive substitution

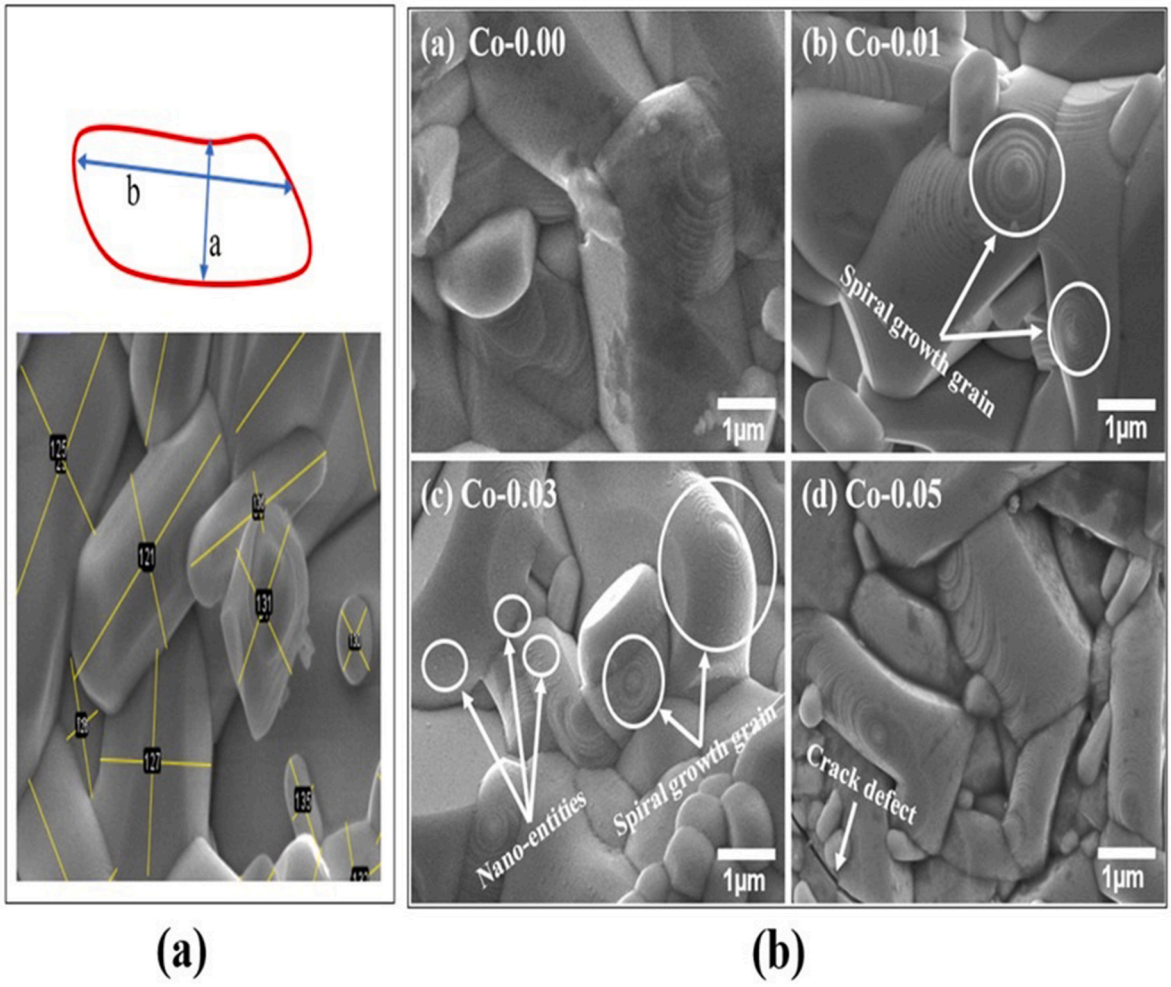

Fig. 4. (a) Grain size measurement technique schematic diagram and image analysis with ImageJ; (b) high-magnification SEM micrographs of Co-doped Y-358 bulk ceramic samples.

disrupts structural coherence and correlates with the degraded transport and magnetic responses observed in the x = 0.05 sample.

3.3. Energy dispersive X-ray spectroscopy

Fig. 5(a–d) shows the Energy-Dispersive X-ray (EDX) spectra of the Y-358 samples annealed in flowing oxygen. Measurements were conducted on representative grain regions to assess local elemental composition and verify cobalt incorporation. All spectra exhibited the expected constituent elements-yttrium (Y), barium (Ba), copper (Cu), cobalt (Co), and oxygen (O), with no extraneous peaks, confirming high chemical purity and the absence of detectable secondary phases. The elemental weight percentages provided in the insets of Fig. 5 indicated that Y, Ba, and O contents remain relatively stable across all compositions, demonstrating that the primary stoichiometry of the Y-358 matrix is preserved.

As anticipated, the Co concentration increases systematically with the nominal doping level, accompanied by a corresponding reduction in Cu content, consistent with partial Cu-site substitution by Co [49]. This substitution is structurally meaningful because Co^{3+} has a smaller ionic radius and a different electronic configuration compared to Cu^{2+}, introducing localized lattice distortions. These distortions are fully consistent with the XRD observations namely, slight *c*-axis elongation, peak broadening, and reduced orthorhombicity, providing strong evidence of effective Co integration into the lattice.

Minor deviations in elemental ratios, such as the slight Y: Cu variation observed for the undoped composition, are attributed to the semi-quantitative nature of point-based EDX analysis. In polycrystalline ceramics, such deviations frequently arise from surface topography, porosity, grain orientation, and localized density variations, all of which

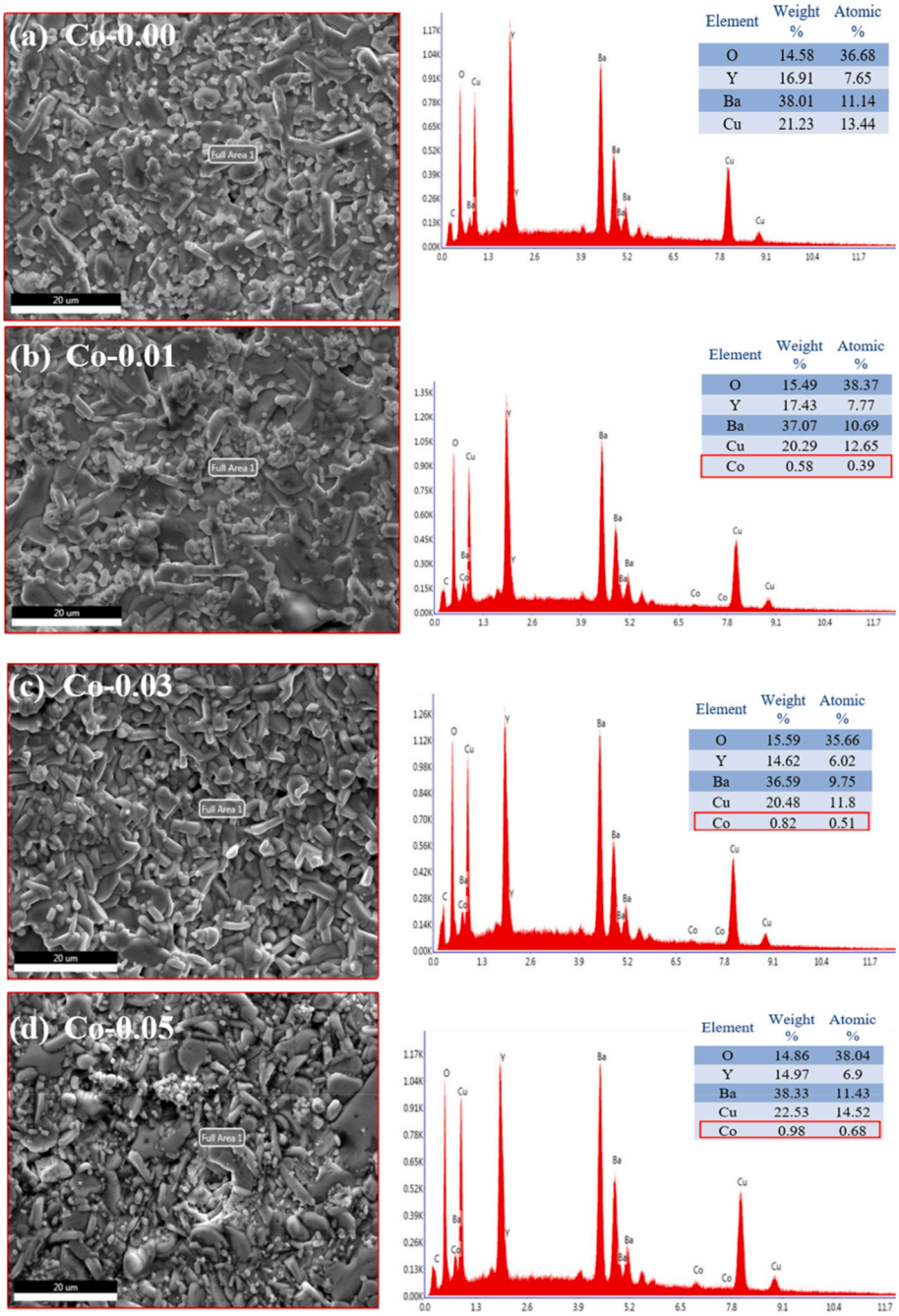

Fig. 5. (a–d) EDX images and tables of the produced samples of Co-doped Y-358 bulk ceramics.

influence X-ray absorption and quantification [21,22,50]. These variations fall within the typical range reported for REBCO systems using spot analysis and do not reflect true bulk compositional inhomogeneity. This interpretation is further supported by the phase-pure XRD patterns (Fig. 2), which show no evidence of segregated impurity phases.

Overall, the EDX results confirm successful Co-for-Cu substitution and reinforce the strong link between compositional modification, induced lattice distortion, and the resulting evolution of superconducting properties. The localized substitutional disorder introduced by Co affects charge-carrier distribution, grain-boundary behavior, and flux-pinning strength, thereby influencing T_c, J_c, and the transport characteristics discussed in the following sections.

3.4. Electrical transport properties

Fig. 6 presents the DC electrical resistivity (R–T) curves of $Y_3Ba_5Cu_{8-x}Co_xO_{18-\delta}$ (x = 0.00, 0.01, 0.03, and 0.05) measured to evaluate the effects of cobalt substitution on the superconducting transport behavior of the Y-358 phase. The temperature-dependent resistivity provides essential information regarding the superconducting transition temperature (T_c), the mean-field transition (T_c^{MF}), and the transition width (ΔT_c), all of which are highly sensitive to lattice modification and microstructural evolution.

Resistivity measurements were performed using the standard four-point probe (4 PP) method within a helium-cooled cryogenic system over the temperature range 30–300 K [7]. Fig. 7 illustrates the measurement configuration, including (a) the schematic diagram of the 4 PP arrangement and (b) the cryogenic sample holder [31]. A constant current was applied through the outer probes while voltage was measured across the inner probes, and resistance was calculated using Ohm's law (R=V/I). Superconducting parameters were extracted through differential analysis of the R–T curves, with $T_{c\text{-onset}}$ determined at the deviation from linear metallic behavior, and $T_{c\text{-zero}}$ defined as the temperature at which resistivity reached zero. T_c^{MF} was identified from the peak in the first derivative ($d\rho/dT$) [41], as shown in Fig. 8. A summary of all extracted values is provided in Table 4. Fig. 9 shows the variation of $T_{c\text{-onset}}$ and $T_{c\text{-zero}}$ as a function of Co doping in the Y-358 system.

The undoped composition (x = 0.00) exhibited the highest $T_{c\text{-onset}}$ (93.25 K) and $T_{c\text{-zero}}$ (86.25 K), corresponding to a narrow transition width (ΔT_c ~7 K), indicative of high phase purity and strong intergranular coupling. Light Co substitution at x = 0.01 and 0.03 preserved metallic behavior above T_c and maintained relatively sharp superconducting transitions. These compositions benefited from improved grain connectivity and moderate lattice strain, as confirmed by SEM and XRD analyses [21]. The optimally substituted sample (x = 0.03) demonstrated the most favorable superconducting response among the doped compositions. Its enhanced behavior is attributed to a balanced interplay between lattice distortion, carrier density, and grain-boundary energetics [31]. Partial substitution of Cu^{2+} by Co^{3+} introduces mild structural distortions that relax the *c*-axis and promote improved oxygen ordering without generating excessive microstrain [23,51]. This controlled modification supports stronger intragrain superconductivity while preserving long-range intergranular coherence [52]. The refined and well-connected grains observed in SEM (Section 3.2) further corroborate the reduced grain-boundary energy and strengthened percolative pathways.

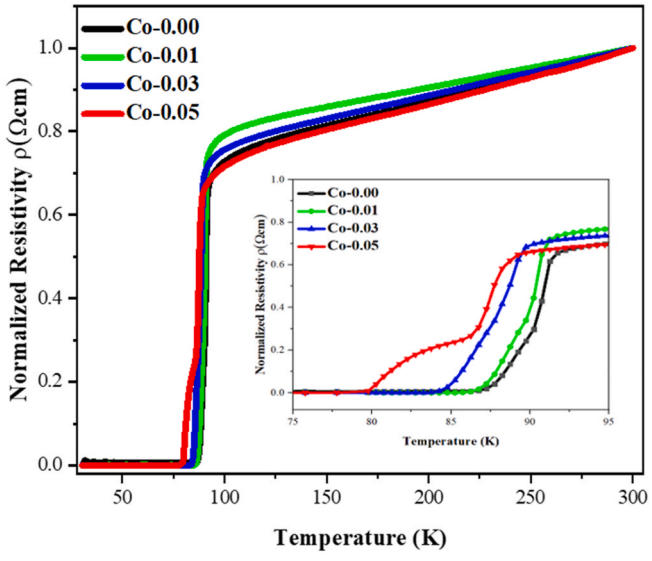

Fig. 6. Electrical resistance as a function of temperature for produced samples of Co-doped Y-358 bulk ceramics.

In contrast, the x = 0.05 sample exhibited a marked deterioration in transport properties, including broader transitions (ΔT_c ~13 K) and significantly reduced $T_{c\text{-zero}}$. The derivative resistivity curves reveal a clear double-step superconducting transition, characteristic of granular systems with weak intergranular coupling [2,31]. The initial drop corresponds to intragrain superconductivity, whereas the second drop reflects delayed intergrain phase coherence mediated by weak-link behavior [10,53]. Although such features might arise from secondary phase impurities, XRD results (Fig. 2) confirmed that impurity levels are similar across all samples. The observed degradation is therefore attributed to microstructural inhomogeneities induced by excessive Co incorporation, specifically porosity, microcracks, and disrupted grain contacts-consistent with the SEM evidence (Fig. 3 (d)). These features are known to fragment percolative paths and force current to traverse weak Josephson junctions, thereby suppressing overall superconducting performance [53,54].

Relative to the findings of Öztürk et al. (2019) [22] (as detailed in Table 4), the present study achieved a notable improvement in the critical temperature onset ($T_{c\text{-onset}}$). Specifically, the Co-0.01 and Co-0.03 samples exhibited enhanced $T_{c\text{-onset}}$ values of 92.25 K and 91.25 K, respectively. In the earlier report, both undoped and Co-doped Y-358 exhibited broader transitions and reduced T_c due to insufficient oxygenation and phase inhomogeneity. In contrast, the current work successfully achieved this enhancement of superconductivity through a refined methodology focusing on four key parameters, (i) enhanced calcination at 910 °C for complete precursor decomposition and improved diffusion [8,40]; (ii) high sintering at 980 °C, promoting densification and improving grain morphology [7,8]; (iii) extended oxygen annealing at 600 °C for 12 h, improving oxygen ordering and hole concentration [1,54]; and (iv) controlled, optimum-level Co substitution, which enhances flux pinning and grain connectivity without disrupting the superconducting [10,55]. The combined structural, microstructural, and transport refinements support a more coherent superconducting network, particularly for the Co-0.03 composition. The effect of Co substitution on hole concentration (p) in the CuO_2 planes was estimated using the empirical relation [56,57]:

$$p = 0.16 - \left[\frac{\left(1 - \frac{T_{c-offset}}{Tc^{max}_{-offset}}\right)}{82.6}\right]^{0.5} \quad (4)$$

These trends highlight the strong sensitivity of the Y-358 phase to carrier depletion caused by Co-for-Cu substitution. Because Co^{3+} introduces local charge compensation, it reduces hole concentration in the CuO_2 planes and shifts the system toward an underdoped regime. Consequently, the evolution of superconductivity reflects a complex interplay between microstructural refinement and carrier reduction. While light substitution (x ≤ 0.03) promotes grain alignment and supports modest flux pinning improvements [33,58], excessive Co incorporation (x = 0.05) results in structural fragmentation, increased

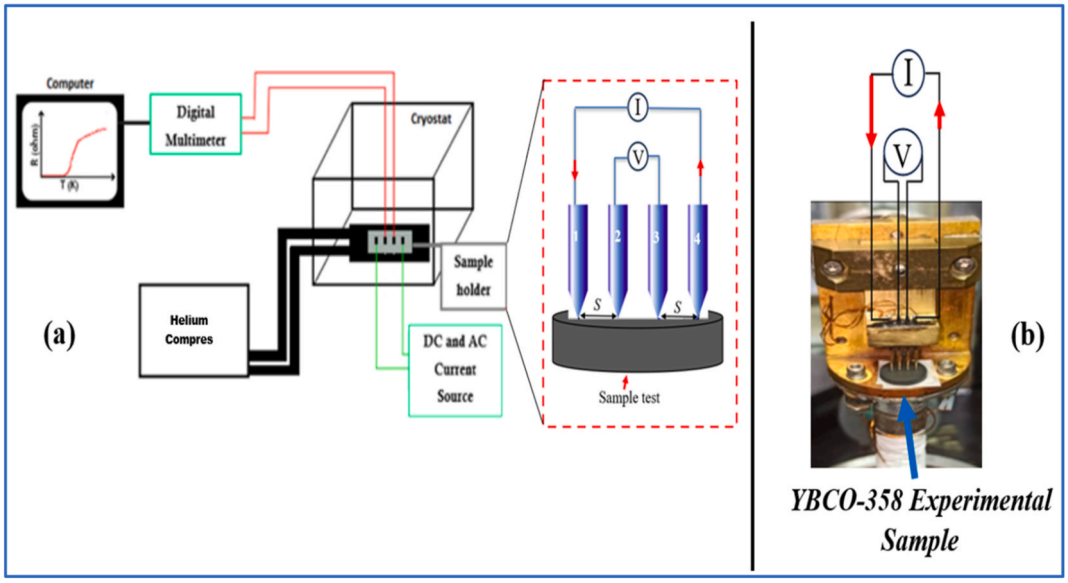

Fig. 7. (a) Schematic diagram of the measurement setup. (b) Experimental sample holder.

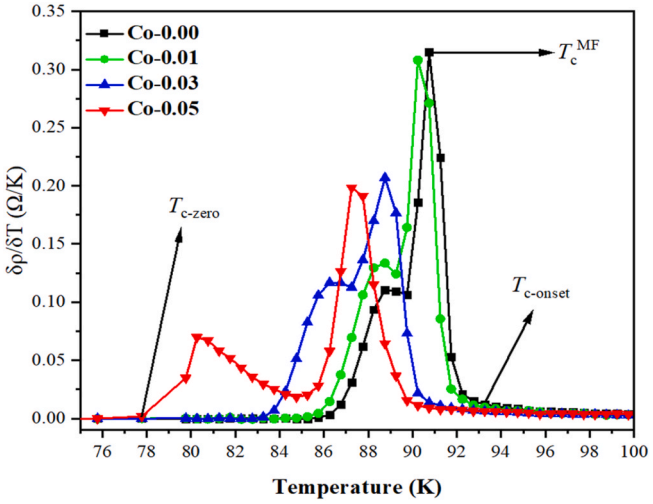

Fig. 8. Shows the temperature derivative of resistivity (dρ/dT) as a function of temperature for Co-doped Y-358 samples.

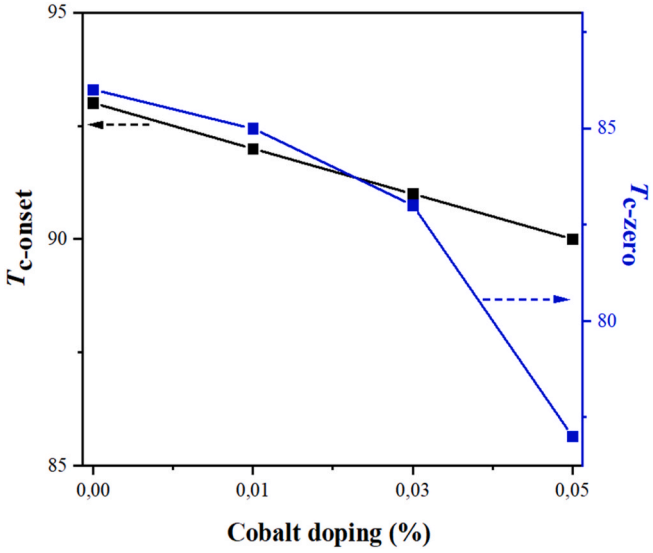

Fig. 9. $T_{c\text{-onset}}$ and $T_{c\text{-zero}}$ vs. cobalt doping in Y-358.

granularity, and suppressed superconductivity.

Overall, the transport characteristics exhibit excellent consistency with the microstructural and compositional trends. At the optimum doping level (x = 0.03), enhanced grain alignment, reduced porosity, and uniform nanoscale features support stable current flow and stronger superconducting coherence. At higher Co levels, microstructural deterioration, including porosity, spiral-like morphologies, and fragmented grains-directly correlates with weakened intergranular conductivity and the emergence of the two-step transition. EDX analysis further confirms progressive Cu depletion with increasing Co content, consistent with partial Co-for-Cu substitution and the associated lattice strain within the CuO_2 planes.

3.5. M − H measurements

3.5.1. M − H hysteresis loops

Understanding the magnetic response of YBCO-based superconductors is essential because substitution-induced structural modifications directly influence diamagnetism, flux pinning, and current-carrying capability. Fig. 10 shows the M − H hysteresis loops of the undoped (Co-0.00) and optimally substituted (Co-0.03) Y-358 samples measured at 20 K under an applied magnetic field range of ±2 T. These two compositions were selected because they represent the baseline material and the sample exhibiting the most notable microstructural and superconducting improvements [9,35].

At high magnetic fields (~±2 T), both loops exhibit non-closure. This behavior is characteristic of Type-II superconductors at temperatures well below the irreversibility field (H_{irr}) and arises from the dominance of irreversible magnetization combined with the intrinsic resolution limitations of the VSM [59,60]. Minor fluctuations in the curves originate from the low sample mass, the intrinsically weak magnetic moment of Y-based cuprates, and subtle intergranular weak-link effects [61,62]. Such features are commonly reported in granular HTS materials and do not affect the validity of the magnetic interpretation derived from the Bean model analysis.

Both samples display the characteristic superconducting hysteresis profile, where the loop width (ΔM) reflects the intragranular flux-pinning strength and the ability of the material to sustain persistent

Table 4
Variation of normal state and superconducting properties with Co doping in Y-358 bulk ceramics.

Samples (Co-%)	$T_{c\text{-onset}}$ (±0.10)	$T_{c\text{-zero}}$ (±0.10)	ΔT_c (±0.14)	P	T_c^{MF}	$\Delta T_c^{MF\text{-zero}}$	Ref.
Co-0.00	93.25	86.25	7.00	0.160	90.75	4.50	This work
Co-0.01	92.75	85.74	7.01	0.148	90.24	4.50	
Co-0.03	91.25	83.25	8.00	0.144	88.75	5.50	
Co-0.05	89.75	77.77	11.98	89.75	87.25	9.48	
Y358-0	92.48	8620.	6.28	/	/	/	Öztürk et al. (2019)
Y358-5	88.22	78.24	9.98	/	/	/	
Y358-10	85.62	72.84	12.78	/	/	/	
Y358-15	83.53	69.81	13.72	/	/	/	

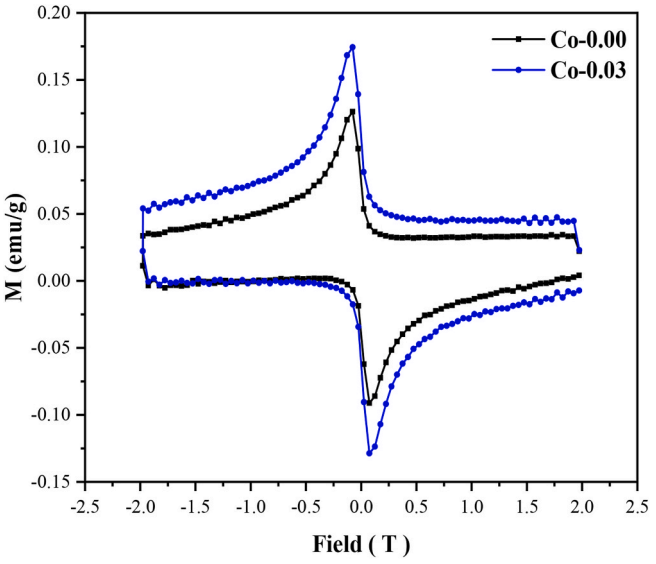

Fig. 10. Magnetization hysteresis (M − H) loops of the undoped Co-0.00 and optimally substituted Co-0.03 of Y-358 samples.

shielding currents. The Co-0.03 sample exhibits a noticeably broader hysteresis and a larger loop area compared to the undoped composition, indicating stronger vortex pinning and a higher effective current-carrying capability. At low substitution levels, Co ions introduce localized structural perturbations within the Cu–O network, modifying vortex lattice spacing, the elastic response of vortices, and the Josephson coupling length between grains [46,63]. These effects collectively strengthen the pinning force in the Y-358 matrix.

As expected, ΔM decreases with increasing magnetic field for both samples due to reduced pinning efficiency at higher vortex densities. Nevertheless, the Co-0.03 specimen consistently retains a larger |M| throughout the entire field range, confirming that controlled low-level Co substitution introduces effective pinning centers that enhance vortex immobilization. These magnetic results strongly corroborate the structural and transport analyses, particularly the improved densification and grain connectivity, and provide direct confirmation of enhanced flux-pinning behavior in the optimally substituted sample.

3.5.2. Critical current density (J_c)

Flux pinning plays a central role in determining the current-carrying capability of Type-II superconductors, as immobilized vortices allow the material to sustain higher critical currents in an applied magnetic field. Substitutional doping in the YBCO lattice is known to introduce point defects, localized strain fields, and nanoscale lattice distortions, all of which serve as effective pinning centers that can enhance the magnetic critical current density (J_c) [9,31,64]. Within the Bean critical-state framework, the magnetic hysteresis width ($\Delta M = M^+ - M^-$) is directly proportional to the intragranular J_c, providing a reliable estimate of vortex-pinning strength [32].

Fig. 11 displays the field-dependent J_c values for the undoped (Co-0.00) and optimally substituted (Co-0.03) Y-358 samples, calculated from the measured M − H loops. Both compositions exhibit the expected monotonic decrease in J_c with increasing magnetic field, reflecting reduced pinning efficiency as vortex density increases. Nevertheless, the Co-0.03 sample consistently maintains higher J_c over the entire field range, demonstrating that controlled low-level Co substitution significantly strengthens vortex immobilization [35,65].

Under zero applied magnetic field, the Co-0.03 sample achieves a maximum J_c of 28.25 kA/cm^2, compared with 21.20 kA/cm^2 for the undoped composition, an enhancement of approximately 33 %. This improvement is consistent with the broader hysteresis width observed in its M − H loop and reflects the formation of additional pinning centers arising from partial Co/Cu substitution. The resulting point defects and local lattice perturbations contribute to vortex trapping within the superconducting grains, thereby enhancing current-carrying capability [21,22]. These findings underline the importance of precise dopant control and microstructural refinement, as even minor variations in compositional distribution can significantly influence J_c.

The J_c enhancement in the Co-0.03 sample is fully aligned with its microstructural characteristics-namely, denser grain packing, reduced porosity, and improved intergranular connectivity, as observed in FESEM analysis. When combined with the resistivity results, the magnetic J_c data provide clear and direct confirmation that low-level cobalt substitution, under optimized thermal processing, effectively enhances flux pinning and superconducting transport efficiency in Y-358 ceramics.

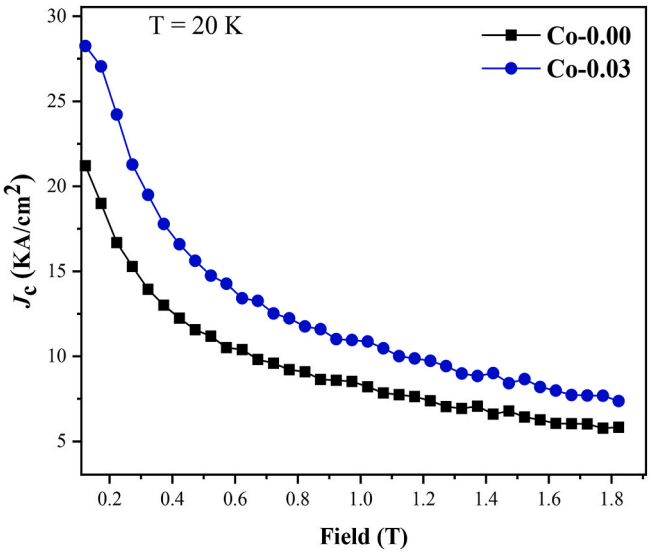

Fig. 11. Field-dependent critical current density (J_c) for the undoped Co-0.00 and Co-0.03 of Y-358 samples, calculated from the Bean critical-state model using the magnetic hysteresis data.

4. Conclusion

In this work, the processing–microstructure–transport relationships of Y-358 ceramics were systematically examined under optimized thermal conditions, with particular emphasis on the influence of low-level cobalt substitution. Structural, microstructural, electrical, and magnetic analyses were performed using XRD, FESEM/EDX, four-point resistivity, and VSM measurements. The key conclusions are as follows:

- XRD analysis confirmed that all compositions preserved the orthorhombic Y-358 phase with no detectable Co-rich secondary phases. Low-level Co substitution (x = 0.01–0.03) produced a slight *c*-axis expansion and reduced orthorhombicity, consistent with localized lattice distortion and oxygen incorporation. At higher substitution (x = 0.05), peak broadening and increased microstrain indicated structural degradation associated with over-doping.
- FESEM observations revealed that the optimum doping (x = 0.03) sample exhibited improved grain alignment, enhanced densification, and stronger intergranular contact. In contrast, the x = 0.05 sample showed abnormal grain growth, porosity, microcracks, clustered nano-entities, and weakened grain-boundary coupling. EDX confirmed the expected Y–Ba–Cu–O matrix with systematic Co-for-Cu substitution and no evidence of elemental segregation.
- Electrical transport (ρ–T) measurements demonstrated superconducting transitions in all samples. The undoped and lightly doped compositions maintained high $T_{c\text{-onset}}$ values (~93–91 K) with narrow ΔT_c, while the optimally substituted x = 0.03 sample demonstrated the strongest intergranular connectivity. The two-step transition observed in the x = 0.05 sample is attributed to reduced carrier concentration and weak-link behavior arising from microstructural deterioration.
- Magnetic hysteresis (M − H) measurements at 20 K revealed significantly stronger flux pinning for the x = 0.03 sample, as evidenced by its wider ΔM. Bean-model analysis confirmed a ~33 % enhancement in J_c from 21.20 kA/cm^2 (x = 0.00) to 28.25 kA/cm^2 (x = 0.03), correlating directly with its refined microstructure and stabilized vortex-pinning landscape.

Building on these findings, the results demonstrate that controlled low-level Co substitution, together with optimized calcination, sintering, and oxygenation, provides an effective pathway to enhance structural stability, grain connectivity, flux pinning, and current-carrying capability in Y-358 ceramics, whereas excessive substitution disrupts lattice integrity and suppresses superconductivity. These insights clarify the dopant–processing interactions governing the Y-358 system and offer a practical route for advancing the functional performance of cuprate superconductors. Future research should prioritize quantitative oxygen-content analysis (e.g., TGA or iodometric titration) to validate carrier-concentration changes, alongside advanced microstructural mapping and broader dopant-optimization studies, to further elucidate the structure–property relationships underlying high-performance Y-358 superconductors.

Statements and declarations

The authors declare that they have no known competing financial interests or personal relationships that could have appeared to influence the work reported in this paper.

Declaration of competing interest

The authors declare that they have no known competing financial interests or personal relationships that could have appeared to influence the work reported in this paper.

Acknowledgments

This research was supported by the Ministry of Higher Education (MOHE) under Fundamental Research Grant Scheme FRGS Grant No. FRGS/1/2026/STG07/UPM/02/4 (5540701) Universiti Putra Malaysia.

References

[1] Arebat RAM, et al. Influence of oxygen flow vs. ambient annealing on microstructure and superconducting properties of $YBa_2Cu_3O_{7-\delta}$ bulk ceramics. J Mater Sci Mater Electron 2025/04/28 2025;36(12):760. https://dx.doi.org/10.1007/s10854-025-14827-7.

[2] Siew Hong Yap MMAK, Fitri Khoerunnisa b, et al. Microstructural and excess conductivity properties of Y-123: effect of organic polymer chitosan inclusion. J Mater Sci Mater Electron 2024/07/22 2024:1452. https://doi.org/10.1007/s10854-024-13161-8.

[3] Kamarudin AN, Awang Kechik Mohd Mustafa Miryala, Pinmangkorn Muralidhar, Murakami Sunsanee, Masato, Kien Chen Soo, Hussein R A Baqiah, Pah Lim Kean, Abdul Halim Shaari. Microstructural, phase formation, and superconducting properties of bulk $YBa_2Cu_3O_y$ superconductors grown by infiltration growth process utilizing the $YBa_2Cu_3O_{y+}$ $ErBa_2Cu_3O_{y+}$ $Ba_3Cu_5O_8$ as a liquid source. Coat 2021;377. https://doi.org/10.3390/coatings11040377.

[4] A. Z. Kh. Oxygen content and disorder effects on the critical current density in $YBa_2Cu_3O_x$. Supercond Sci Technol 2001;14(1):30. 2001/01/01, https://dx.doi.org/10.1088/0953-2048/14/1/305.

[5] Salama K, Mironova M, Stolbov S, Sathyamurthy S. Grain boundaries in bulk YBCO. Phys C Supercond 2000;341–348:1401–5. https://doi.org/10.1016/S0921-4534(00)00957-6. 2000/11/01/.

[6] Ozturk O, Asikuzun E, Yildirim G. The role of Lu doping on microstructural and superconducting properties of $Bi_2Sr_2CaLu_xCu_2O_y$ superconducting system. J Mater Sci Mater Electron 2013/04/01 2013;24(4):1274–81. https://doi.org/10.1007/s10854-012-0918-z.

[7] Arebat RAM, et al. Impact of calcination temperature on the microstructure and superconductivity of $YBa_2Cu_3O_{7-\delta}$ ceramic prepared via modified thermal decomposition method. J. Aust. Ceram. Soc. 2025;61(4):1375–86. https://doi.org/10.1007/s41779-025-01172-5.

[8] Dihom MM, et al. Effects of calcination temperature on microstructure and superconducting properties of Y123 ceramic prepared using thermal treatment method. Solid State Phenom 2017;268:325–9. https://dx.doi.org/10.4028/www.scientific.net/SSP.268.325.

[9] Ozturk O, Guducu G, Kurnaz S, Seydioglu T, Safran S. Structural and mechanical dynamics of Y-358 superconductors influenced by Tb/Y and Zn/Cu substitutions. J Supercond Nov Magnetism 2024/12/27 2024;38(1):38. https://doi.org/10.1007/s10948-024-06865-9.

[10] Slimani Y, Hannachi E, Azzouz FB, Salem MB. Comparative study of the effect of magnetic nanoparticle $CoFe_2O_4$ on fluctuation-induced conductivity of Y-123 and Y-358 superconductors. J Supercond Nov Magnetism 2019/03/01 2019;32(3):511–9. https://doi.org/10.1007/s10948-018-4746-0.

[11] Dihom MM, et al. Calcium-substituted $Y_3Ba_5Cu_8O_{18}$ ceramics synthesized via thermal treatment method: structural and superconducting properties. J Supercond Nov Magnetism 2019;32:1875–83.

[12] Maw Kuen W, et al. Superconductivity at 93 K in a new mixed-phase Y-Ba-Cu-O compound system at ambient pressure. Phys Rev Lett 1987;58:908.

[13] Yanagisawa K, Matsui Y, Kodama Y, Yamada Y, Matsumoto T. High-resolution transmission electron microscope study of effects of cobalt substitution on the stability and perfection of $YBa_2Cu_4O_y$ superconductors. Phys C Supercond 1991;183(4–6):197–206.

[14] Khan NA, Mazhar M, Maqsood A. A novel method for the direct synthesis of the $Y_2Ba_4Cu_7O_{15-x}$ superconductor. Supercond Sci Technol 2002;15(4):577.

[15] Udomsamuthirun P, Kruaehong T, Nilkamjon T, Ratreng S. The new superconductors of YBaCuO materials. J Supercond Nov Magnetism 2010;23:1377–80.

[16] Topal U, Akdogan M, Ozkan H. Electrical and structural properties of $RE_3Ba_5Cu_8O_{18}$ (RE= Y, Sm and Nd) superconductors. J Supercond Nov Magnetism 2011;24:2099–102.

[17] Gholipour S, et al. Structural phase of Y358 superconductor comparison with Y123. J Supercond Nov Magnetism 2012;25:2253–8.

[18] Pimentel J, et al. Synthesis and characterization of the superconductors $Y_3Ba_5Cu_{8-x}$ Fe_xO_{18} ($0.0597 \leq x \leq 0.1255$). J Supercond Nov Magnetism 2015;28:509–12.

[19] Aliabadi A, Farshchi YA, Akhavan M. A new Y-based HTSC with Tc above 100 K. Phys C (Amsterdam, Neth) 2009;469(22):2012–4.

[20] Ozturk O, et al. Effect of Co/Cu partial replacement on fundamental features of Y-123 ceramics. J Mater Sci Mater Electron 2020;31:7630–41.

[21] Ozturk O, et al. Evolution of fundamental mechanical properties with aliovalent Co/Cu partial substitution and preparation method for Y-123 system. J Mater Sci Mater Electron 2024/05/28 2024;35(15):1018. https://doi.org/10.1007/s10854-024-12740-z.

[22] Ozturk O, et al. Investigation of structural, superconducting and mechanical properties of Co/Cu substituted YBCO-358 ceramic composites. J Mater Sci Mater Electron 2019/04/01 2019;30(8):7400–9. https://dx.doi.org/10.1007/s10854-019-01053-1.

[23] Lin CT, Li SX, Zhou W, Mackenzie A, Liang WY. Cobalt-doped YBCO single crystals and their accurate characterisation. Phys C Supercond 1991/05/15/1991;176(1):285–94. https://doi.org/10.1016/0921-4534(91)90725-E.

[24] Chamekh S, Bouabellou A. The effects of magnetic dopant on the structural and electrical properties in superconducting $YBaCu_3O_{7-\delta}$ ceramic. Adv Chem Eng Sci 2018;8(1):1. https://dx.doi.org/10.4236/aces.2018.81001.

[25] Liyanawaduge NP, Kumar Singh S, Kumar A, Awana VPS, Kishan H. Superconducting and magnetic properties of Zn-doped $YBa_2Cu_3O_{7-\delta}$. J Supercond Nov Magnetism 2011/07/01 2011;24(5):1599–605. https://doi.org/10.1007/s10948-010-1063-7.

[26] Singhal RK. How the substitution of Zn for Cu destroys superconductivity in YBCO system? J Alloys Compd 2010/04/09/2010;495(1):1–6. https://doi.org/10.1016/j.jallcom.2010.01.106.

[27] Yang CY, et al. X-ray absorption near-edge studies of substitution for Cu in $YBa_2(Cu_{1-x})_3O_{7-\delta}$ (M=Fe, Co, Ni, and Zn). Phys Rev B 1990;42(4):2231–41. https://doi.org/10.1103/PhysRevB.42.2231.

[28] Liu C, et al. Influence of the Eu substitution on the structure and magnetic properties of the Sr-hexaferrites. Ceram Int 2020/01/01/2020;46(1):171–9. https://doi.org/10.1016/j.ceramint.2019.08.245.

[29] Liu C, et al. Characterizations of magnetic transition behavior and electromagnetic properties of Co-Ti co-substituted SrM-based hexaferrites $SrCo_xTi_xFe_{12-2x}O_{19}$ compounds. J Alloys Compd 2019/05/05/2019;784:1175–86. https://doi.org/10.1016/j.jallcom.2019.01.112.

[30] Yap SH, et al. Comparing study of electrical transport properties of bulk Y-123 synthesized by modified wet and dry synthesis methods. Solid State Sci Technol 2025/04/09/2025:107921. https://doi.org/10.1016/j.solidstatesciences.2025.107921.

[31] Arebat RA, et al. Sm_2O_3-induced superconductivity enhancements in bulk Y-123 ceramics synthesized via a novel modified thermal decomposition method. J Mater Res Technol 2025. https://doi.org/10.1016/j.jmrt.2025.05.065. 2025/05/19/.

[32] Bean CP. Magnetization of high-field superconductors. Rev Mod Phys 1964;36(1):31–9. https://doi.org/10.1103/RevModPhys.36.31.

[33] Güdücü G, et al. Assessment of superconducting and structural stability of advanced Y-123 and Y-358 ceramics with Tb/Y substitution in main matrices. J Alloys Compd 2024;997:174838.

[34] Slimani Y, et al. Comparative study of nano-sized particles $CoFe_2O_4$ effects on superconducting properties of Y-123 and Y-358. Phys B Condens Matter 2014;450:7–15.

[35] Güdücü G, et al. Assessment of superconducting and structural stability of advanced Y-123 and Y-358 ceramics with Tb/Y substitution in main matrices. J Alloys Compd 2024;997:174838. https://doi.org/10.1016/j.jallcom.2024.174838. 2024/08/30/.

[36] Chamekh S, Bouabellou A. The effects of magnetic dopant on the structural and electrical properties in superconducting $YBaCu_3O_{7-\delta}$ ceramic. Adv Chem Eng Sci 2018;8(1):1–10.

[37] Gupta S, Yadav R, Lalla N, Verma G, Das B. Microstructural and superconducting properties of $YBa_2Cu_{3-x}Co_xO_{7-\delta}$ system. Integrated Ferroelectrics Int J 2010;116(1):68–81.

[38] Xue R, Dai H, Chen Z, Li T, Xue Y. Effects of Zn doping on crystal structure, Raman spectra and superconductivity of $SmBa_2Cu_3O_{7-\delta}$ systems. Mater Sci Eng, B 2013/04/01/2013;178(6):363–7. https://doi.org/10.1016/j.mseb.2013.01.004.

[39] Xiao G, Bakhshai A, Cieplak MZ, Tesanovic Z, Chien CL. Correlation between superconductivity and normal-state properties in the $La_{1.85}$ $Sr_{0.15}Cu_{1-x}Zn_xO_4$ system. Phys Rev B 1989;39(1):315–21. https://doi.org/10.1103/PhysRevB.39.315.

[40] Arebat RAM, Kechik MMA. $YBa_2Cu_3O_{7-d}$ bulk superconductors: exploring the impact of two synthesis techniques on the microstructure and critical temperature. Solid State Sci Technol 2024;32(2). https://myjms.mohe.gov.my/index.php/masshp/article/view/25985. 28-41ISSN 0128-7389.

[41] Arebat RAM, et al. Enhancing superconducting properties of $YBa_2Cu_3O_{7-\delta}$ through Nd_2O_3 addition prepared using modified thermal decomposition method. Appl Phys 2024/11/18 2024;130(12):897. https://dx.doi.org/10.1007/s00339-024-08035-z.

[42] Suan MSM, Johan MR, Siang TC. Synthesis of $Y_3Ba_5Cu_8O_{18}$ superconductor powder by auto-combustion reaction: effects of citrate–nitrate ratio. Phys C Supercond 2012;480:75–8.

[43] Barood F, et al. Orthorhombic $YBa_2Cu_3O_{7-\delta}$ superconductor with TiO_2 nanoparticle addition: crystal structure, electric resistivity, and AC susceptibility. Coat 2023;13(6):1093. https://doi.org/10.3390/coatings13061093.

[44] Peh HK, et al. Enhancement of critical current density in Mg incorporated ex-situ MgB_2 via co-addition of B_4C and Dy_2O_3. J Alloys Compd 2025;1012:178233.

[45] Sah NAMIA, et al. Comparative studies of pure $YBa_2Cu_3O_{7-\delta}$ prepared by modified thermal decomposition method against thermal treatment method. Appl Phys 2024/04/25 2024;130(5):340. https://dx.doi.org/10.1007/s00339-024-07412-y.

[46] Slimani Y, et al. Comparative investigation of the ball milling role against hand grinding on microstructure, transport and pinning properties of $Y_3Ba_5Cu_8O_{18\pm\delta}$ and $YBa_2Cu_3O_{7-\delta}$. Ceram Int 2018;44(16):19950–7.

[47] Yap SH, et al. Fluctuation induces conductivity and microstructural studies in Y-123: effect of CaO inclusion. J Alloys Compd 2024:175955.

[48] Yap SH, et al. Microstructural and excess conductivity properties of Y-123: effect of organic polymer chitosan inclusion. J Mater Sci Mater Electron 2024;35(21):1452.

[49] Sengupta LC, Roughani B, Aubel J, Sundaram S, Joiner WCH. Effect of substitutional doping on phonon spectra of $YBa_2(Cu_{1-x}Co_x)_3O_{7-\delta}$. Phys C Supercond 1990/01/01/1990;165(1):125–30. https://doi.org/10.1016/0921-4534(90)90442-H.

[50] Yildirim G. Beginning point of metal to insulator transition for Bi-2223 superconducting matrix doped with Eu nanoparticles. J Alloys Compd 2013;578:526–35.

[51] Liu L, Dong C, Zhang J, Li J. The microstructure study of Co-doped YBCO system. Phys C Supercond 2002/09/01/2002;377(3):348–56. https://doi.org/10.1016/S0921-4534(01)01286-2.

[52] Jurelo AR, et al. Coherence transition in granular high temperature superconductors. Phys C Supercond 1999/01/01/1999;311(1):133–9. https://doi.org/10.1016/S0921-4534(98)00617-0.

[53] Salamati H, Kameli P. Effect of deoxygenation on the weak-link behavior of $YBa_2Cu_3O_{7-\delta}$ superconductors. Solid State Commun 2003/02/01/2003;125(7):407–11. https://doi.org/10.1016/S0038-1098(02)00809-8.

[54] Yap SH, et al. Fluctuation induces conductivity and microstructural studies in Y-123: effect of CaO inclusion. J Alloys Compd 2024/11/15/2024;1005:175955. https://doi.org/10.1016/j.jallcom.2024.175955.

[55] Elizabeth S, Anand A, Bhat SV, Subramanyam SV, Bhat HL. Influence of cobalt doping on superconducting transition in as-grown YBCO single crystals. Solid State Commun 1999/01/04/1999;109(5):333–8. https://doi.org/10.1016/S0038-1098(98)00553-5.

[56] Tranquada JM, Heald S, Moodenbaugh A, Xu Y. Mixed valency, hole concentration, and T_c in $YBa_2Cu_3O_{6+x}$. Phys Rev B 1988;38(13):8893.

[57] Tallon JL, Bernhard C, Shaked H, Hitterman R, Jorgensen J. Generic superconducting phase behavior in high-T_c cuprates: t_c variation with hole concentration in $YBa_2Cu_3O_{7-\delta}$. Phys Rev B 1995;51(18):12911.

[58] Tran DH, et al. Superconductivity in $Bi_{1.6}Pb_{0.4}Sr_2Ca_2Cu_3O_{10+\delta}$ ceramics with cobalt ferrite ($CoFe_2O_4$) nanoparticle addition. Ceram Int 2025.

[59] Navau C, et al. Critical state in finite type-II superconducting rings. Phys Rev B 2005;71(21):214507. https://doi.org/10.1103/PhysRevB.71.214507.

[60] Shantsev DV, Galperin YM, Johansen TH. Thin superconducting disk with field-dependent critical current: magnetization and ac susceptibilities. Phys Rev B 2000;61(14):9699–706. https://doi.org/10.1103/PhysRevB.61.9699. 04/01/.

[61] Harres A, et al. Criteria for saturated magnetization loop. J Magn Magn Mater 2016/03/15/2016;402:76–82. https://doi.org/10.1016/j.jmmm.2015.11.046.

[62] Navau C, Del-Valle N, Sanchez A. Macroscopic modeling of magnetization and levitation of hard Type-II superconductors: the critical-state model. IEEE Trans Appl Supercond 2013;23(1):8201023. https://doi.org/10.1109/TASC.2012.2232916. 8201023.

[63] Wei K, Abd-Shukor R. Superconducting and transport properties of (Bi-Pb)-Sr-Ca-Cu-O with Nano-Cr_2O_3 additions. J Electron Mater 2007/12/01 2007;36(12):1648–51. https://doi.org/10.1007/s11664-007-0287-1.

[64] Agarwal AGM. Miryala, "Enhancing the superconducting properties of bulk (Sm, Eu,Gd)$Ba_2Cu_3O_{7-\delta}$: impact of BaO_2 and Ag_2O addition via infiltration growth process in air,". J Appl Phys 2025. https://dx.doi.org/10.1063/5.0248525.

[65] Lucas B, et al. Magnetic and levitation properties of YBCO/polymer composite drop-casting films. Next Mater 2025;8:100789. https://doi.org/10.1016/j.nxmate.2025.100789.